Chiral spin liquids on the kagome lattice with projected entangled simplex states

Sen Niu [1,*] Juraj Hasik,[2] Ji-Yao Chen [3,4,†] and Didier Poilblanc [1]

[1]*Laboratoire de Physique Théorique, C.N.R.S. and Université de Toulouse, 31062 Toulouse, France*
[2]*Institute for Theoretical Physics, University of Amsterdam, Science Park 904, 1098 XH Amsterdam, The Netherlands*
[3]*School of Physics, Sun Yat-sen University, Guangzhou 510275, China*
[4]*Dahlem Center for Complex Quantum Systems, Freie Universität Berlin, Berlin 14195, Germany*

The infinite projected entangled simplex state (iPESS), a type of tensor network (TN) state, has been used successfully for simulating and characterizing *nonchiral* spin liquids on the kagome lattice. Here, we demonstrate that iPESS also provides a faithful representation of a *chiral* spin liquid (CSL) on the same lattice, namely the ground state of the spin-1/2 kagome Heisenberg antiferromagnet with a scalar chirality. By classifying local tensors according to SU(2) and point group symmetries, we construct a chiral ansatz breaking reflection P and time reversal T symmetries while preserving PT. The variational TN states are shown to host, for bond dimension $D \geqslant 8$, a chiral gapless entanglement spectrum following $SU(2)_1$ conformal field theory. The correlation function shows a small weight long-range tail complying with the prediction of the TN bulk-edge correspondence. We identify a nonchiral manifold spanned by only a subset of symmetric tensors where a new emergent *tensor conservation law* is realized. This allows us to both probe the stability of the nonchiral spin liquid and discuss its transition to CSL induced by a scalar chirality term.

Introduction. Quantum spin liquids have received numerous attention in condensed matter theory and experiments due to their exotic properties such as fractionalized excitations and long-range entanglement [1,2]. A prominent system is the kagome Heisenberg antiferromagnet (KHA) where the quantum ground state is nonmagnetic. Promising ground states were proposed such as the algebraic U(1) spin liquid with Dirac spinon spectrum [3] and the gapped spin liquid with $\mathbb{Z}_2$ topological order [4]. By perturbing such system with a scalar spin chirality term or longer-range Heisenberg couplings, a more intriguing chiral spin liquid (CSL) state can be stabilized as uncovered by density-matrix renormalization group studies in quasi-one dimension [5,6]. CSL states were proposed by Kalmeyer and Laughlin in spin models as a bosonic variant of some fractional quantum Hall state [7]. Such states host anyonic quasiparticles [8] in the bulk as well as chiral gapless modes [9] on the edge described by $(1 + 1)$-dimensional conformal field theories (CFT).

In recent decades, tensor network (TN) states [10] have emerged as a powerful framework for investigating strongly correlated systems both analytically and numerically. They encode many-body state into a network of local tensors contracted by their connected virtual bonds. In two dimensions, TN states can represent several well-known *nonchiral* spin liquid states exactly, e.g., the toric code state with $\mathbb{Z}_2$ topological order [11,12], the string-net states [13], and the short-range resonating valence bond (RVB) states on the kagome lattice (with $\mathbb{Z}_2$ topological order) and on the square lattice [being gapless and with U(1) gauge symmetry] [14]. On the numerical side, TN states have also proven their

competitiveness against other numerical methods [15] in determining the nature of ground states of challenging models such as the KHA [16,17].

In contrast to the case of nonchiral topological states where TN representation works well with local gauge symmetry imposed [12,18], it is less clear whether TN states can represent generic chiral topological states [19–21]. In the past, a lot of effort has been devoted to construct CSL states on the square lattice [22–28] with symmetric [23,29] infinite projected entangled pair states (iPEPS) [30,31]. These constructions include two important ingredients. First, both the reflection P and time reversal T symmetries are broken while the combined PT symmetry is preserved. On the square lattice with C_{4v} point group symmetry, one can choose the real elementary tensors transforming according to A_1 and A_2 irreducible representations (IRREPs) [23], and the $A_1 + iA_2$ chiral ansatz then satisfies the symmetry condition exactly. Second, appropriate spins should be assigned in the virtual space. For the simplest $SU(2)_1$ CSL (bosonic $\nu = 1/2$ Laughlin state), the virtual space is chosen as a direct sum $\mathcal{V} = 0 \oplus 1/2$ where two virtual spins 0 and 1/2 correspond to two primary fields of Wess-Zumino-Witten (WZW) $SU(2)_1$ CFT and the local tensor satisfies the necessary gauge symmetry [22]. This heuristic rule for virtual spins turns out to be valid also for $SU(N)_1$ [26] and non-Abelian $SU(2)_2$ [28] CSLs.

However, generalizing the construction to the nonbipartite kagome lattice is not straightforward. The natural extension of iPEPS on the kagome lattice [32] was named infinite projected entangled simplex state (iPESS) [33]. A direct adoption of the heuristic rule fails for the simplest $SU(2)_1$ case as the trivalent tensor ansatz $A_1 + iA_2$ with virtual space $\mathcal{V} = 0 \oplus 1/2$ yields the nonchiral short-range RVB state [14]. Here the phase i only contributes a global phase to the many-body state due to an emergent conservation law for the total number of A_1

*sen.niu@irsamc.ups-tlse.fr
†chenjiy3@mail.sysu.edu.cn

tensors on the lattice. One then has to generalize the heuristic rule by including more relevant virtual spins while keeping the gauge symmetry intact in the local tensors. The main purpose of this paper is to provide the first example of a two-dimensional TN (iPESS) construction of CSL states on the kagome lattice. We start from the Hamiltonian, which hosts a CSL ground state.

Model and classification of symmetric iPESS. We consider the nearest-neighbor spin-1/2 KHA model with a scalar spin chirality term $\chi_{ijk} = \mathbf{S}_i \cdot (\mathbf{S}_j \times \mathbf{S}_k)$ acting on both up and down triangles
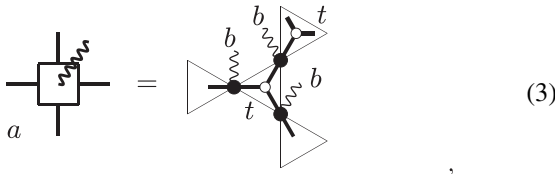
$$H = J_H \sum_{\langle i,j \rangle} \mathbf{S}_i \cdot \mathbf{S}_j + J_\chi \sum_{i,j,k \in \triangle, \triangledown} \chi_{ijk}, \qquad (1)$$

with sites i, j, k on triangles ordered clockwise. The χ_{ijk} term breaks P and T symmetries, while preserving SU(2) spin rotation and PT symmetries. For convenience, we define $J_\chi / J_H = \tan \theta$ and set $J_H = 1$. The $\theta = 0$ point then corresponds to the T-symmetric KHA point.

We construct the iPESS ansatz for a translationally invariant state on the kagome lattice from two unique tensors: An on-site tensor b, which resides on physical sites and a trivalent tensor t, which resides in triangles. Using Penrose notation, b and t have the form

$$b = \;\rule[0.5ex]{1.5em}{0.4pt}\!\!\!\bullet\!\!\rule[0.5ex]{1em}{0.4pt}\;, \quad t = \;\bigwedge\;. \qquad (2)$$

Here, the on-site b tensor has one physical index (wavy line) of dimension 2 corresponding to spin-1/2 and two virtual indices (solid lines) of dimension D running over states in the virtual space $\mathcal{V}$, while the trivalent tensor t has three virtual indices of dimension D. Kagome lattice is tiled with t tensors, each connected by three b tensors to neighboring t's as shown below. For evaluating the physical observables, we group three adjacent b tensors and two t tensors into an iPEPS tensor a defined as

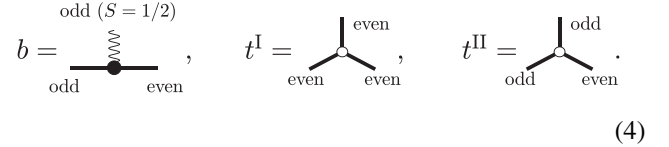$$\raisebox{-1em}{\includegraphics{fig3}} \qquad (3)$$

mapping the wave function to an effective square lattice where each unit cell contains three spins. We adopt the corner transfer matrix renormalization (CTMRG) method [34,35], controlled by environment dimension χ, to contract the resulting TN approximately (exact in the $\chi \to \infty$ limit).

To further restrict the ansatz, we impose both point group symmetries and SU(2) symmetry on both b and t tensors ensuring that the many-body state preserves lattice symmetries and is a global spin singlet. The latter requires a choice of an appropriate virtual space $\mathcal{V}$ for the CSL state, which we obtain from simple update simulations [16,36] at $\theta = 0.2\pi$, deep in the CSL phase [5]. Starting from a $D = 6$ ansatz with $\mathcal{V} = 0 \oplus \frac{1}{2} \oplus 1$ [16,37] and appropriate point group quantum number (see below) we perform the imaginary time evolution while keeping SU(2) symmetry. The resulting optimal virtual spaces $\mathcal{V} = \oplus_{i=1}^{D^*} \mathcal{V}_i$ for various multiplet dimension D^* are shown in Table I. The product virtual space $\mathcal{V}^{\otimes 2}$ for b ($\mathcal{V}^{\otimes 3}$

TABLE I. Virtual spaces $\mathcal{V}$ for different multiplet dimensions D^* and numbers of distinct elementary tensors resolved by point group symmetry (see text).

D^*	D	Virtual space	b_A	b_B	$t_{A_1}^I$	$t_{A_1}^{II}$	$t_{A_2}^I$	$t_{A_2}^{II}$
2	3	$0 \oplus \frac{1}{2}$	1	1	1	0	0	1
3	6	$0 \oplus \frac{1}{2} \oplus 1$	2	2	1	2	1	1
4	8	$0 \oplus \frac{1}{2} \oplus 1 \oplus \frac{1}{2}$	4	4	2	4	1	4
5	12	$0 \oplus \frac{1}{2} \oplus 1 \oplus \frac{1}{2} \oplus \frac{3}{2}$	5	5	2	7	1	7

for t) tensor can be decomposed into disconnected subspaces labeled by the occupations $\{n_1, ..., n_{D^*}\}$ with the constraint $\sum_i n_i = 2$ ($\sum_i n_i = 3$). Importantly, due to SU(2) invariance the total occupations for even (integer) virtual spins n_{even} and odd (half-integer) virtual spins n_{odd} are constrained. The b tensors satisfy $\{n_{\text{even}}, n_{\text{odd}}\} = \{1, 1\}$ due to the physical spin $S = 1/2$. For the t tensor, $\{n_{\text{even}}, n_{\text{odd}}\}$ can be either $\{3, 0\}$ (dubbed as t^I) or $\{1, 2\}$ (dubbed as t^{II}). Graphically these tensors take the form

$$b = \overset{\text{odd }(S=1/2)}{\underset{\text{odd}\qquad\text{even}}{\bigvee}}, \quad t^I = \overset{\text{even}}{\underset{\text{even}\quad\text{even}}{\bigwedge}}, \quad t^{II} = \overset{\text{odd}}{\underset{\text{odd}\quad\text{even}}{\bigwedge}}. \qquad (4)$$

The conservation of the total *parity* for b and t tensors infers a $\mathbb{Z}_2$ gauge symmetry to our family of TN states.

Finally, we impose point group symmetries C_2 on b and C_{3v} on t tensors with respect to permutation of virtual indices. The b tensors are divided into b_A and b_B, transforming as symmetric A and antisymmetric B IRREPs of the C_2 group. Similarly, t tensors are further divided into $t_{A_1}^I$, $t_{A_2}^I$, $t_{A_1}^{II}$, $t_{A_2}^{II}$, where A_1, A_2 are reflection symmetric and antisymmetric IRREPs of the C_{3v} group. The complete set of these real-valued elementary tensors can be obtained from the diagonalization procedure proposed in Ref. [23]. We show the number of these elementary tensors in each subspace in Table I.

Now we are ready to construct the many-body chiral/nonchiral states by defining b and t tensor as superposition of elementary tensors. For b we consider only b_A elementary tensors, since they are equivalent to b_B via a virtual $\mathbb{Z}_2$ gauge transformation [38] and their superposition breaks lattice rotation symmetry. The existence of reflection symmetry then depends only on the choice of the t tensors. There are two types of nonchiral states constructed from (i) pure A_1 or pure A_2 IRREP tensors or (ii) $t_{A_1}^I + e^{i\phi} t_{A_2}^{II}$ or $t_{A_1}^{II} + e^{i\phi} t_{A_2}^I$ tensors, ϕ being an (irrelevant) arbitrary number. The nonchiral ansatz (ii) preserves reflection symmetry due to an emergent *conservation law* for the number of A_1 tensors on the lattice: Every b tensor has one odd virtual index and, on the lattice with a fixed number of physical sites, the number of odd virtual indices is also fixed. Therefore, the number of t^{II} tensors is conserved and the $e^{i\phi}$ factor only changes the global phase of the many-body state. The ansatz for chiral states should allow for fluctuations of the number of $t_{A_1}^I$ and $t_{A_2}^{II}$ tensors, which is realized by choosing $t_{A_1}^I + t_{A_1}^{II} + i t_{A_2}^I + i t_{A_2}^{II}$ (dubbed as $A_1 + iA_2$), which is invariant under PT operation.
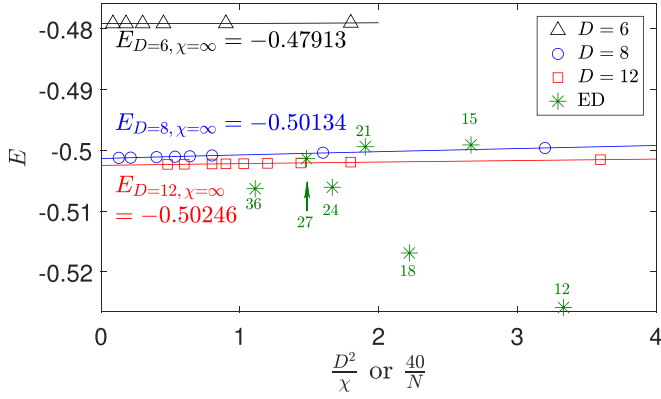
FIG. 1. Energies of the $A_1 + iA_2$ chiral iPESS at $\theta = 0.2\pi$ as functions of CTMRG environment dimension χ. The states are optimized at $\chi = 40, 60, 120$ for $D = 6, 8, 12$. The ED energies on clusters with sizes ($N = 12, 15, 18, 21, 24, 27, 36$) are marked by green symbols.

CSL state in the iPESS representation. Here we demonstrate that the topological CSL state can be represented by the $A_1 + iA_2$ chiral iPESS by determining it variationally at $\theta = 0.2\pi$, deep in the CSL phase. In our optimization scheme, the b and t tensors are written as linear superpositions with real coefficients of the elementary tensors of Table I. These coefficients are the variational parameters and we optimize them by gradient descent method, where the gradients are obtained from finite differences of energy evaluated by CTMRG at fixed χ. The energies at $D = 6, 8, 12$ in Fig. 1 show that the ground-state energy converges quickly. By comparing with the exact diagonalization (ED) energies on finite-size clusters (up to 36 sites) we find that already from $D \geqslant 8$ the chiral iPESS ansatz has very good energy.

In order to identify the topological nature of optimized states, we compute the bipartite entanglement spectrum (ES) as proposed by Li and Haldane [39]. Here, the iPEPS tensors a of Eq. (3) are put on an infinitely long cylinder with finite circumference N_v. The entanglement spectrum of the TN state can then be calculated exactly by ED for small N_v [14,40] and approximately with the CTMRG method [25,28,41] for larger N_v. We find that a satisfactory agreement is reached between the ES of $D \geqslant 8$ states and the predictions of $SU(2)_1$ CSL [42]. The results of ES for the $D = 8$ variational state are displayed in Fig. 2. The levels are labeled by momentum and total spin quantum numbers. One can see the low-lying chiral branches disperse linearly and the levels in the even/odd sector match those of two $SU(2)_1$ conformal towers associated to spin $0/\frac{1}{2}$ primary WZW fields as marked in Fig. 2. Moreover, the agreement with the CFT level counting becomes better for larger N_v. Further details regarding computation of ES and finite-size dependence of its two topological sectors can be found in the Appendix.

After analysis of the boundary properties of our CSL iPESS we turn to a second important aspect, the bulk correlations. In all previous studies, done exclusively on the square lattice, CSLs described by iPEPS display weak long-range tails in bulk correlations [22–28], contrary to the expectation for a gapped CSL phase. We show the same behavior arises also in bulk correlations on the kagome lattice, depicted in
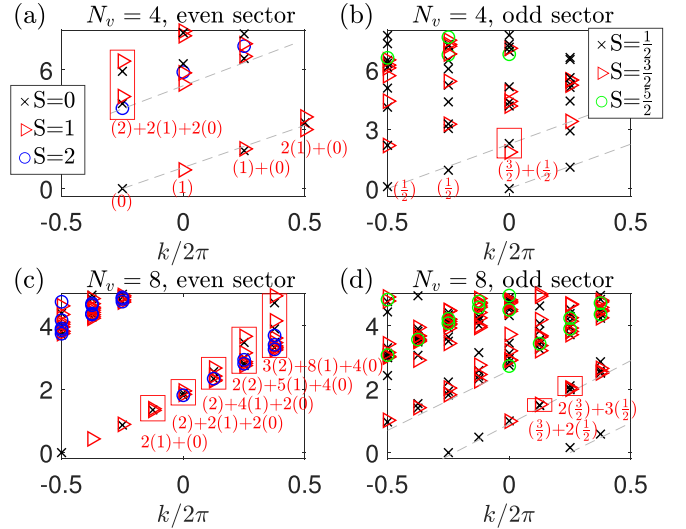

FIG. 2. Entanglement spectrum of the optimized $A_1 + iA_2$ chiral iPESS ($D = 8$) at $\theta = 0.2\pi$ with even/odd sectors normalized separately. [(a),(b)] ES on width $N_v = 4$ cylinders obtained by ED. [(c),(d)] ES on $N_v = 8$ cylinders obtained from CTMRG with $\chi = 40$. The levels marked by red boxes agree with the level counting of the $SU(2)_1$ WZW CFT.

Fig. 3 for $D = 8$ state. Spin and dimer correlation functions clearly show two distinct regimes. At short distance $r \leqslant 4$ the spin correlations decay exponentially with very short correlation length $\xi_{bulk} \approx 0.6$, which is believed to be related to the bulk gap of the true ground state [27,28]. At longer distances a long-range tail of tiny magnitude ($\approx 10^{-6}$) emerges. Its decay becomes slower than any exponential function as its correlation length increases with χ. To confirm this we analyze the transfer matrix spectrum [43] in Figs. 3(c) and 3(d), which demonstrates that by increasing χ, the gap in the spectrum $|\lambda_0| - |\lambda_1|$ (normalization $|\lambda_0| = 1$ is used) vanishes
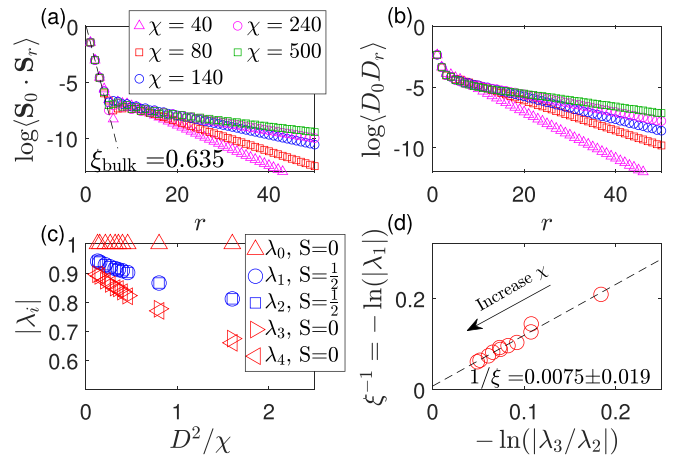

FIG. 3. Bulk correlations in the optimized $A_1 + iA_2$ chiral iPESS ($D = 8$) at $\theta = 0.2\pi$. [(a),(b)] Connected spin and dimer correlation functions where $D_i = \mathbf{S}_i \cdot \mathbf{S}_{i+1}$ with increasing CTMRG environment dimension χ. (c) Normalized SU(2) multiplet eigenvalues λ_i of the transfer matrix. The gap of the spectrum $|\lambda_0| - |\lambda_1|$ scales to zero in the large χ limit. (d) Scaling of the leading correlation length ξ.
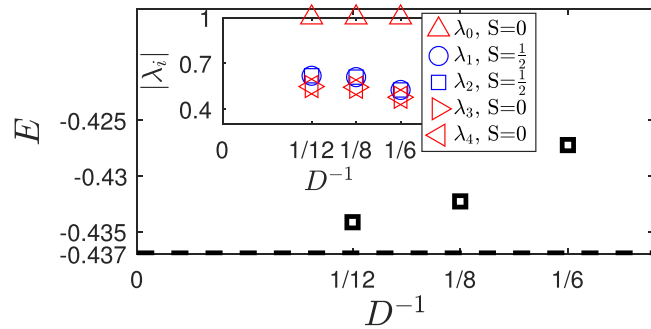
FIG. 4. The variational energies of the nonchiral $t_{A_1}^I + t_{A_2}^{II}$ ansatz at the KHA point. The dashed line shows the best energy -0.4369 in Ref. [16] with $D = 29$ ($D^* = 12$). Inset shows the transfer matrix eigenvalues for different D.
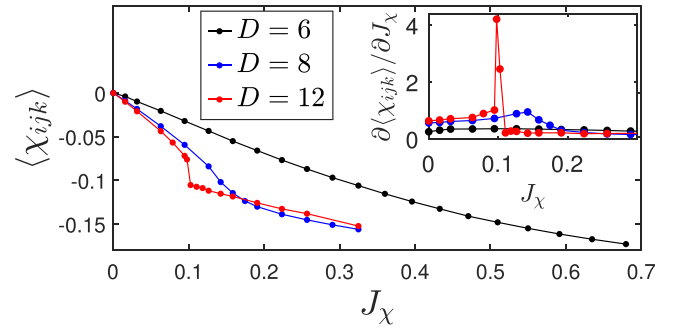

FIG. 5. The observable $\langle \chi_{ijk} \rangle$ of the optimized chiral states. Here $\chi = 60$ is used. Inset shows the first-order derivatives.

and the leading correlation length $\xi = -1/\ln|\lambda_1|$ (associated with the tail) diverges. The dimer correlations behave similarly. These long-range tails indicate the state supports some form of long-range bulk correlations, which still could decay faster than any power law (see discussion in Ref. [24]). These features come as a direct consequence of the no-go theorem [19–21] formally preventing the exact finite-D TN representation of gapped chiral topological states. This can be physically understood from the PEPS bulk-edge correspondence: The entanglement Hamiltonian necessary for harboring an ideal gapless chiral ES, strictly speaking, must be of infinite range which, in turn, implies an infinite bulk correlation length [14,40]. These features closely resemble those observed in the iPEPS representations of CSL on the square lattice [24,27], strongly suggesting a universal finite-D artifact in all TN ansatze of spin-1/2 CSL. Good variational energies, sharply defined chiral ES branches, and exponentially decaying correlations at short distances clearly demonstrate the ability of iPESS developed here to simulate CSL phases on the kagome lattice. We conjecture that the unphysical weak long-distance gossamer tail will eventually vanish upon increasing D. In the Appendix we show the same CSL features are obtained from iPESS simulations without symmetries, which indicates that the CSL phase in the iPESS representation is not fine tuned.

The KHA point and the transition to the CSL phase. We now construct the optimal *point group symmetric* ansatz at the KHA $J_\chi = 0$ point and investigate the possible occurrence of spontaneous time-reversal symmetry breaking induced by the proximity to the CSL phase [6,44–46]. Starting the optimizations from random $A_1 + iA_2$ chiral states we find they always flow to the nonchiral $t_{A_1}^I + t_{A_2}^{II}$ ansatz (the same as the $D = 3$ RVB state), which is a subset of the complete family of chiral ansatze. This suggests that spontaneous time-reversal symmetry breaking does not occur at the KHA point. As shown in Fig. 4, the variational energies of our finite-D nonchiral ansatze are consistent with the finite D energies obtained in Ref. [16] where only SU(2) symmetry is imposed, hence validating our fully symmetric ansatz. At currently accessible $D = 6, 8, 12$ the resulting iPESS is gapped and has $\mathbb{Z}_2$ topological order [16] (in contrast to the Gutzwiller-projected Dirac liquid of similar energy [15]). The large gap seen in the transfer matrix spectrum shown in the inset of Fig. 4 implies that, at current D, the correlation

length is short and a larger D may still be needed to approach the true ground state. However, our knowledge of the exact form of the optimal ansatz is expected to greatly speed up the variational optimization at larger D.

To investigate the transition between the CSL phase at large J_χ and the nonchiral spin liquid phase at $J_\chi = 0$, we look at the scalar chirality $\langle \chi_{ijk} \rangle$ in the optimized ansatz, as shown in Fig. 5. A linear growth of $|\langle \chi_{ijk} \rangle|$ is observed at small J_χ, consistent with linear response theory and a finite value of the chiral susceptibility $\chi_{\text{chiral}} = -\partial \langle \chi_{ijk} \rangle / \partial J_\chi |_{J_\chi = 0}$ (measured by the slope at $J_\chi \to 0$). For $D \geqslant 8$ a singularity builds up at finite J_χ, as reflected more clearly by the behavior of the first (numerical) derivative of $|\langle \chi_{ijk} \rangle|$ with respect to J_χ suggesting a first-order transition around $J_\chi \simeq 0.1$, in agreement with the DMRG result in Ref. [47]. The transition detected from the jump of $\langle \chi_{ijk} \rangle$ is also confirmed by behaviors of the variational parameters and the ES, see the Appendix. Note the value of the critical point may be overestimated since the gap of the variational state at the KHA point decreases with increasing D making the system more susceptible to stabilize the CSL phase.

Conclusion and outlook. In this paper, we demonstrated that the CSL ground state of the chiral Heisenberg model on the kagome lattice can be represented faithfully by the chiral iPESS ansatz. By classifying elementary tensors with optimal virtual spaces using SU(2) and point group symmetries, we constructed an enlarged family of chiral states for numerical simulations (including a nonchiral subset) and studied the transition induced by the scalar chirality term between the nonchiral spin liquid phase and the CSL phase. In contrast to the former, the latter is characterized by a well-defined chiral edge mode consistent with the SU(2)$_1$ conformal field theory. A long-range tail (of very small weight) in the spin-spin correlation is found, as also encountered in the square lattice CSL analog [24,27], suggesting universality in finite-D artifacts of TN representation of CSL. The nonchiral ansatz discovered here paves the way for the symmetric variational optimization and the study of the excitation spectrum at the KHA point. Also, it would be interesting to apply our chiral ansatz to explore spontaneous time-reversal symmetry breaking in the model with longer range couplings [6,44–46].
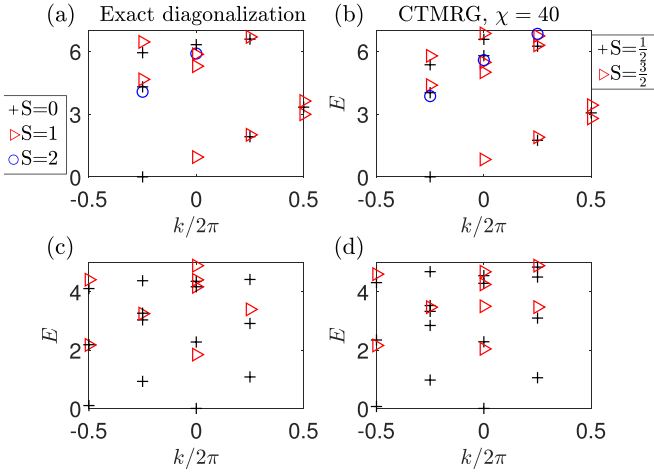
FIG. 6. Entanglement spectrum of the optimized $A_1 + iA_2$ chiral ansatz ($D = 8$) at $\theta = 0.2\pi$ computed on a $N_v = 4$ infinitely-long cylinder. [(a),(c)] ED. [(b),(d)] CTMRG with $\chi = 40$. The even (first row) and odd (second row) sectors are normalized separately.

APPENDIX

1. CSL entanglement spectrum on finite-circumference cylinders

In the main text we used two methods, i.e., ED (exact contraction) and CTMRG, to obtain the boundary operators needed to calculate the ES on a (bipartitioned) infinite cylinder of finite circumference N_v, see Fig. 2. The second method, which is approximate but applicable to larger N_v, is tested here by comparing its results to the one obtained by ED on the same thin cylinder ($N_v = 4$). As shown in Figs. 6(a)–6(d) using the $D = 8$ ansatz, a perfect agreement is found both for even and odd sectors in the low-energy regime.

The finite-circumference dependence of the two sectors of the ES can be seen in Fig. 7. We observe a systematic even/odd effect depending on the parity of $N_v/2$: for $N_v = 4m$ ($m \in \mathbb{N}^+$) the ES in the even sector has larger weight (lower energy) while for $N_v = 4m + 2$ the ES in the odd sector has larger weight (lower energy). We conjecture that this is because the leading sector in the two-site entanglement Hamiltonian is the odd sector. Moreover, we find the leading sector only has one dispersion branch while the subleading sector has two nearly-degenerate branches shifted by π in momentum as can be seen in Fig. 7.
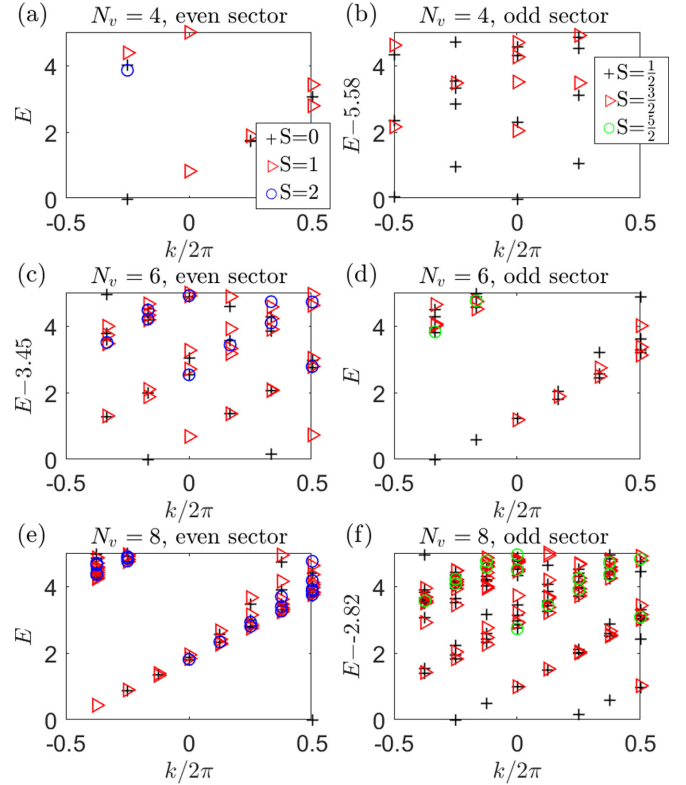

FIG. 7. Entanglement spectrum of the optimized $A_1 + iA_2$ chiral ansatz ($D = 8$) at $\theta = 0.2\pi$. CTMRG boundary tensors with $\chi = 40$ are used. The even and odd sectors are normalized together. For $N_v = 4m$ the leading sector is the even sector, while for $N_v = 4m + 2$ the leading sector is the odd sector, as reflected from the offsets on the energy axis introduced in (b), (c), and (f) (to move the ground state down to $E = 0$)

2. Unconstrained iPESS simulation of the CSL state

Here we show that the kagome CSL state can also be obtained from simulations without symmetry constraints, similar to the case on the square lattice [27]. In this calculation, we still consider the same parameter $\theta = 0.2\pi$, and perform gradient optimization with the gradient obtained from an automatic difference algorithm [51,52]. The $D = 8$ state is optimized at $\chi = 64$ and further evaluated at $\chi = 128$. The energy per site $E = -0.5018$ is only slightly better than the energy of the symmetric ansatz, via forming a small mag-
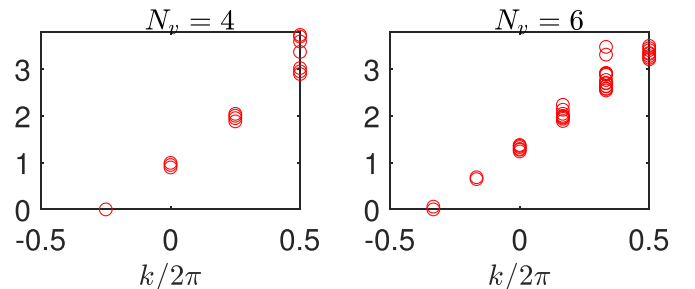

FIG. 8. Entanglement spectrum of the optimized unconstrained $D = 8$ iPESS at $\theta = 0.2\pi$. The fixed point boundary operators are obtained from CTMRG $\chi = 40$.
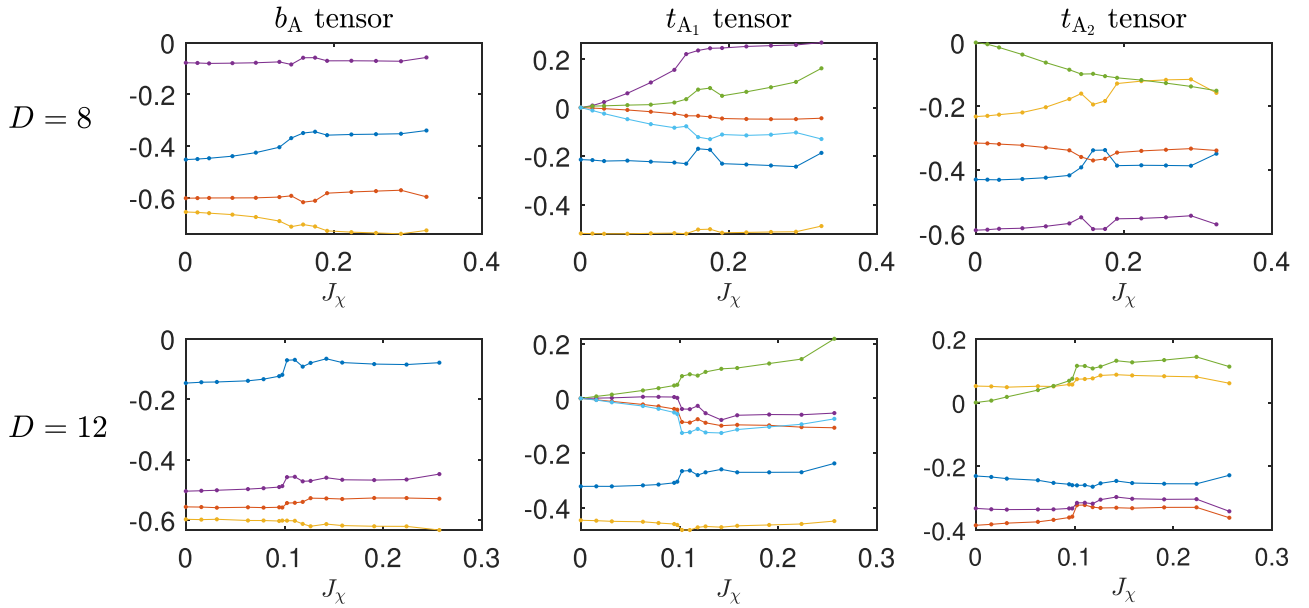
FIG. 9. Optimized variational parameters associated to the b_A, t_{A_1}, and t_{A_2} tensors vs J_χ. At the $J_\chi = 0$ point, the parameters defining the $t_{A_1}^{II}$, $t_{A_2}^{I}$ tensors vanish exactly (the optimal ansatz there is the reflection symmetric ansatz $t_{A_1}^{I} + t_{A_2}^{II}$). When J_χ is turned on, these parameters grow linearly up to the critical point.

netization around 5×10^{-3}. This feature of CSL phase is in sharp contrast to the kagome spin liquid at the KHA point where the finite D energy can be improved a lot through forming considerable mean-field like magnetization [16,17]. The ES for the unconstrained simulation is shown in Fig. 8. As the SU(2) symmetry is slightly broken, the spin quantum number is not well defined and we can not distinguish topological sectors. Nevertheless, the dispersion is perfectly linear and the degeneracies of low-energy states agree well with those in the leading sectors in Fig. 7. We also find

that the correlation functions have the same long-range features as the symmetric states in the main text (not shown here).

3. Behavior of the variational parameters across the phase transition

Apart from the chirality observable $\langle \chi_{ijk} \rangle$ displayed in the main text, the phase transition from tuning J_χ is also reflected in the behavior of the variational parameters defining the tensors, as can be seen in Fig. 9. Before the transition, the

FIG. 10. Entanglement spectrum of the optimized $A_1 + iA_2$ chiral ansatz ($D = 8$) at different J_χ. $N_v = 4$ and CTMRG $\chi = 40$ are used. [(a),(d)] ES at the KHA point with $J_\chi = 0$. [(b),(e)] ES below the $D = 8$ critical J_χ point. [(c),(f)] ES above the $D = 8$ critical J_χ point.
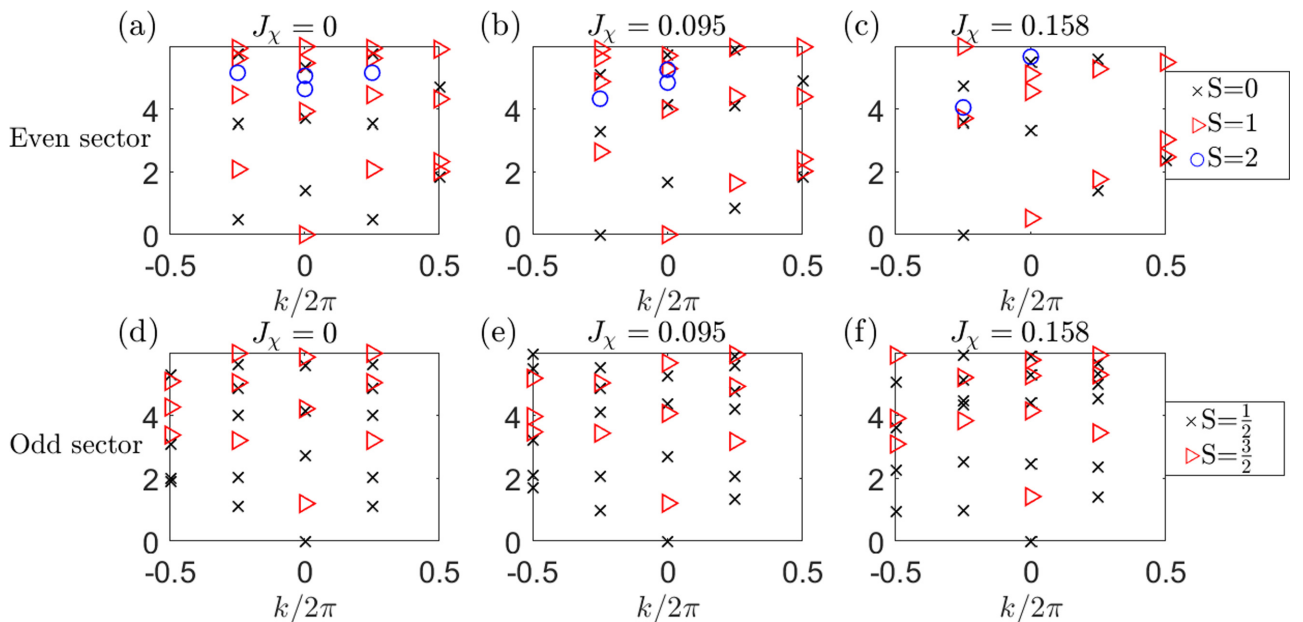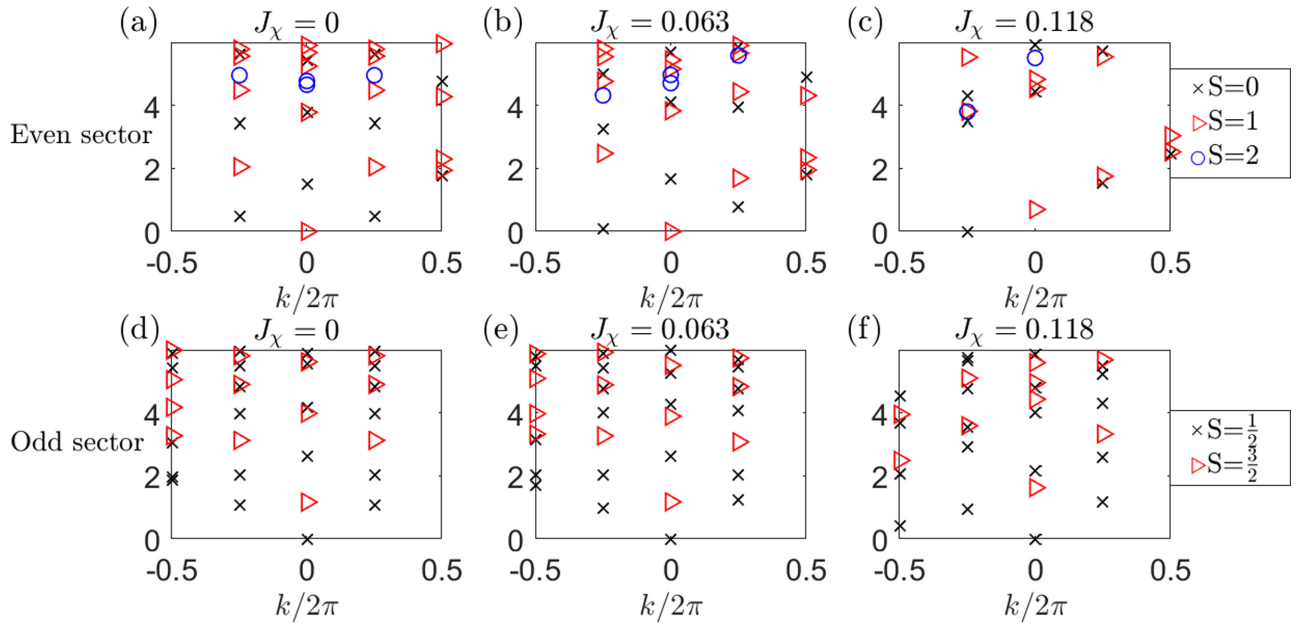
FIG. 11. Entanglement spectrum of the optimized $A_1 + iA_2$ chiral ansatz ($D = 12$) at different J_χ. $N_v = 4$ and CTMRG $\chi = 40$ are used. [(a),(d)] ES at the KHA point with $J_\chi = 0$. [(b),(e)] ES below the $D = 12$ critical J_χ point. [(c),(f)] ES above the $D = 12$ critical J_χ point.

parameters vary smoothly and the parameters associated to the $t_{A_1}^{II}, t_{A_2}^{I}$ tensors grow from zero linearly. At the transition point, some of the parameters show clear jumps (e.g., the parameters in $t_{A_1}^{II}$ tensors at $D = 12$). Below and above the transition, the parameters have two distinct behaviors, which is consistent with the level crossing picture in first-order phase transition.

4. Behavior of the entanglement spectrum across the phase transition

The two phases can be further distinguished from their ES. First, we show the ES at the KHA point $J_\chi = 0$ for $D = 8, 12$ in Figs. 10(a) and 10(b) and in Figs. 11(a) and 11(b). The quantum numbers and dispersions are essentially the same as the $D = 3$ short-range RVB state given in Ref. [14], as can be expected from the fact that the SU(2) symmetric variational state at finite (small) D has $\mathbb{Z}_2$ topological order

[16]. We further show the ES for J_χ values below and above the (estimated) critical value of the transition for $D = 8$ in Figs. 10(c)–10(f) and for $D = 12$ in Figs. 11(c)–11(f). It is clear that the ES in the leading sector (even sector for $N_v = 4$ here) show a qualitative change compared to the nonchiral case. Once J_χ is turned on, while still below the transition, there is no separation between low- and high-energy states and the lowest entanglement energy level is a $S = 1$ triplet (although reflection symmetry is broken). Above the transition, the low energy chiral branches become well separated from the higher energy states with the lowest level being a $S = 0$ singlet. For the subleading sector (odd sector for $N_v = 4$ here), which has smaller weight, as there exists two branches, the transition is not so clear. We expect the transition in the subleading sector will become more visible for larger cylinder circumferences N_v.

[1] L. Savary and L. Balents, Quantum spin liquids: A review, Rep. Prog. Phys. **80**, 016502 (2017).

[2] Y. Zhou, K. Kanoda, and T.-K. Ng, Quantum spin liquid states, Rev. Mod. Phys. **89**, 025003 (2017).

[3] Y. Ran, M. Hermele, P. A. Lee, and X.-G. Wen, Projected-Wave-Function Study of the Spin-1/2 Heisenberg Model on the Kagomé Lattice, Phys. Rev. Lett. **98**, 117205 (2007).

[4] S. Sachdev, Kagomé- and triangular-lattice Heisenberg antiferromagnets: Ordering from quantum fluctuations and quantum-disordered ground states with unconfined bosonic spinons, Phys. Rev. B **45**, 12377 (1992).

[5] B. Bauer, L. Cincio, B. P. Keller, M. Dolfi, G. Vidal, S. Trebst, and A. W. Ludwig, Chiral spin liquid and emergent anyons in a kagome lattice Mott insulator, Nat. Commun. **5**, 5137 (2014).

[6] S.-S. Gong, W. Zhu, and D. Sheng, Emergent chiral spin liquid:

Fractional quantum hall effect in a kagome Heisenberg model, Sci. Rep. **4**, 6317 (2014).

[7] D. C. Tsui, H. L. Stormer, and A. C. Gossard, Two-Dimensional Magnetotransport in the Extreme Quantum Limit, Phys. Rev. Lett. **48**, 1559 (1982).

[8] B. I. Halperin, Statistics of Quasiparticles and the Hierarchy of Fractional Quantized Hall States, Phys. Rev. Lett. **52**, 1583 (1984).

[9] X.-G. Wen, Gapless boundary excitations in the quantum Hall states and in the chiral spin states, Phys. Rev. B **43**, 11025 (1991).

[10] F. Verstraete, V. Murg, and J. I. Cirac, Matrix product states, projected entangled pair states, and variational renormalization group methods for quantum spin systems, Adv. Phys. **57**, 143 (2008).

[11] F. Verstraete, M. M. Wolf, D. Perez-Garcia, and J. I. Cirac, Criticality, the Area Law, and the Computational Power of Projected Entangled Pair States, Phys. Rev. Lett. **96**, 220601 (2006).

[12] N. Schuch, I. Cirac, and D. Pérez-García, PEPS as ground states: Degeneracy and topology, Ann. Phys. **325**, 2153 (2010).

[13] Z.-C. Gu, M. Levin, B. Swingle, and X.-G. Wen, Tensor-product representations for string-net condensed states, Phys. Rev. B **79**, 085118 (2009).

[14] D. Poilblanc, N. Schuch, D. Pérez-García, and J. I. Cirac, Topological and entanglement properties of resonating valence bond wave functions, Phys. Rev. B **86**, 014404 (2012).

[15] Y. Iqbal, F. Becca, S. Sorella, and D. Poilblanc, Gapless spin-liquid phase in the kagome spin-$\frac{1}{2}$ Heisenberg antiferromagnet, Phys. Rev. B **87**, 060405(R) (2013).

[16] J.-W. Mei, J.-Y. Chen, H. He, and X.-G. Wen, Gapped spin liquid with Z_2 topological order for the kagome Heisenberg model, Phys. Rev. B **95**, 235107 (2017).

[17] H.-J. Liao, Z.-Y. Xie, J. Chen, Z.-Y. Liu, H.-D. Xie, R.-Z. Huang, B. Normand, and T. Xiang, Gapless Spin-Liquid Ground State in the S = 1/2 Kagome Antiferromagnet, Phys. Rev. Lett. **118**, 137202 (2017).

[18] N. Schuch, D. Poilblanc, J. I. Cirac, and D. Perez-Garcia, Topological Order in the Projected Entangled-Pair States Formalism: Transfer Operator and Boundary Hamiltonians, Phys. Rev. Lett. **111**, 090501 (2013).

[19] T. B. Wahl, H.-H. Tu, N. Schuch, and J. I. Cirac, Projected Entangled-Pair States Can Describe Chiral Topological States, Phys. Rev. Lett. **111**, 236805 (2013).

[20] S. Yang, T. B. Wahl, H.-H. Tu, N. Schuch, and J. I. Cirac, Chiral Projected Entangled-Pair State with Topological Order, Phys. Rev. Lett. **114**, 106803 (2015).

[21] J. Dubail and N. Read, Tensor network trial states for chiral topological phases in two dimensions and a no-go theorem in any dimension, Phys. Rev. B **92**, 205307 (2015).

[22] D. Poilblanc, J. I. Cirac, and N. Schuch, Chiral topological spin liquids with projected entangled pair states, Phys. Rev. B **91**, 224431 (2015).

[23] M. Mambrini, R. Orús, and D. Poilblanc, Systematic construction of spin liquids on the square lattice from tensor networks with SU(2) symmetry, Phys. Rev. B **94**, 205124 (2016).

[24] D. Poilblanc, Investigation of the chiral antiferromagnetic Heisenberg model using projected entangled pair states, Phys. Rev. B **96**, 121118(R) (2017).

[25] J.-Y. Chen, S. Capponi, A. Wietek, M. Mambrini, N. Schuch, and D. Poilblanc, SU(3)$_1$ Chiral Spin Liquid on the Square Lattice: A View from Symmetric Projected Entangled Pair States, Phys. Rev. Lett. **125**, 017201 (2020).

[26] J.-Y. Chen, J.-W. Li, P. Nataf, S. Capponi, M. Mambrini, K. Totsuka, H.-H. Tu, A. Weichselbaum, J. von Delft, and D. Poilblanc, Abelian SU(N)$_1$ chiral spin liquids on the square lattice, Phys. Rev. B **104**, 235104 (2021).

[27] J. Hasik, M. Van Damme, D. Poilblanc, and L. Vanderstraeten, Simulating Chiral Spin Liquids with Projected Entangled-Pair States, Phys. Rev. Lett. **129**, 177201 (2022).

[28] J.-Y. Chen, L. Vanderstraeten, S. Capponi, and D. Poilblanc, Non-Abelian chiral spin liquid in a quantum antiferromag-

[29] net revealed by an iPEPS study, Phys. Rev. B **98**, 184409 (2018).

[29] S. Jiang and Y. Ran, Symmetric tensor networks and practical simulation algorithms to sharply identify classes of quantum phases distinguishable by short-range physics, Phys. Rev. B **92**, 104414 (2015).

[30] F. Verstraete and J. I. Cirac, Renormalization algorithms for quantum-many body systems in two and higher dimensions, arXiv:cond-mat/0407066.

[31] J. Jordan, R. Orús, G. Vidal, F. Verstraete, and J. I. Cirac, Classical Simulation of Infinite-Size Quantum Lattice Systems in Two Spatial Dimensions, Phys. Rev. Lett. **101**, 250602 (2008).

[32] N. Schuch, D. Poilblanc, J. I. Cirac, and D. Pérez-García, Resonating valence bond states in the PEPS formalism, Phys. Rev. B **86**, 115108 (2012).

[33] Z.-Y. Xie, J. Chen, J. F. Yu, X. Kong, B. Normand, and T. Xiang, Tensor Renormalization of Quantum Many-Body Systems Using Projected Entangled Simplex States, Phys. Rev. X **4**, 011025 (2014).

[34] T. Nishino and K. Okunishi, Corner transfer matrix renormalization group method, J. Phys. Soc. Jpn. **65**, 891 (1996).

[35] P. Corboz, T. M. Rice, and M. Troyer, Competing States in the t-J Model: Uniform d-Wave State Versus Stripe State, Phys. Rev. Lett. **113**, 046402 (2014).

[36] H. C. Jiang, Z. Y. Weng, and T. Xiang, Accurate Determination of Tensor Network State of Quantum Lattice Models in Two Dimensions, Phys. Rev. Lett. **101**, 090603 (2008).

[37] S. Jiang, P. Kim, J. H. Han, and Y. Ran, Competing spin liquid phases in the S = $\frac{1}{2}$ Heisenberg model on the kagome lattice, SciPost Phys. **7**, 006 (2019).

[38] A. Hackenbroich, A. Sterdyniak, and N. Schuch, Interplay of SU(2), point group, and translational symmetry for projected entangled pair states: Application to a chiral spin liquid, Phys. Rev. B **98**, 085151 (2018).

[39] H. Li and F. D. M. Haldane, Entanglement Spectrum as a Generalization of Entanglement Entropy: Identification of Topological Order in Non-Abelian Fractional Quantum Hall Effect States, Phys. Rev. Lett. **101**, 010504 (2008).

[40] J. I. Cirac, D. Poilblanc, N. Schuch, and F. Verstraete, Entanglement spectrum and boundary theories with projected entangled-pair states, Phys. Rev. B **83**, 245134 (2011).

[41] D. Poilblanc, N. Schuch, and I. Affleck, SU(2)$_1$ chiral edge modes of a critical spin liquid, Phys. Rev. B **93**, 174414 (2016).

[42] Note the ES computed at $D = 6$ does not show the CSL features, lacking well separated linear branches.

[43] T. Nishino, K. Okunishi, and M. Kikuchi, Numerical renormalization group at criticality, Phys. Lett. A **213**, 69 (1996).

[44] Y.-C. He and Y. Chen, Distinct Spin Liquids and Their Transitions in Spin-1/2 XXZ Kagome Antiferromagnets, Phys. Rev. Lett. **114**, 037201 (2015).

[45] Y.-C. He, D. N. Sheng, and Y. Chen, Chiral Spin Liquid in a Frustrated Anisotropic Kagome Heisenberg Model, Phys. Rev. Lett. **112**, 137202 (2014).

[46] R.-Y. Sun, H.-K. Jin, H.-H. Tu, and Y. Zhou, Possible chiral spin liquid state in the $s = 1/2$ kagome Heisenberg model, arXiv:2203.07321

[47] R. Haghshenas, S.-S. Gong, and D. N. Sheng, Single-layer tensor network study of the Heisenberg model with chiral

interactions on a kagome lattice, Phys. Rev. B **99**, 174423 (2019).

[48] A. Weichselbaum, Non-Abelian symmetries in tensor networks: A quantum symmetry space approach, Ann. Phys. **327**, 2972 (2012).

[49] A. Weichselbaum, X-symbols for non-Abelian symmetries in tensor networks, Phys. Rev. Res. **2**, 023385 (2020).

[50] J. Haegeman, TensorKit.jl: A Julia package for large-scale tensor computations, with a hint of category theory., https://github.com/Jutho/TensorKit.jl.

[51] H.-J. Liao, J.-G. Liu, L. Wang, and T. Xiang, Differentiable Programming Tensor Networks, Phys. Rev. X **9**, 031041 (2019).

[52] J. Hasik and G. Mbeng, peps-torch: A differentiable tensor network library for two-dimensional lattice models, https://github.com/jurajHasik/peps-torch.